RSC Advances

PAPER

View Article Online
View Journal | View Issue

Cite this: *RSC Adv.*, 2020, **10**, 19185

Modifying structural polymorphs and tuning electronic properties in pressure-stabilized binary Ir–Sb phases

Siyuan Liu,[a] Dan Zhou,*[bc] Manai Cui,[a] Jing Xu,[a] Xuejiao Ma,[a] Yuheng Cheng,[a] Zhexue Jin*[d] and Yanhui Liu *[a]

The search for novel structures and chemical stoichiometry of binary Ir–Sb compounds is of great importance in view of their catalytic applications. Based on the results of swarm structure searching technique combined with density functional theory, we proposed the hitherto unknown Ir–Sb phase diagram in a wide pressure range with various chemical compositions. Besides two ambient pressure phases of $IrSb_3$-Im$\bar{3}$ and $IrSb_2$-$P2_1/c$, five novel phases of IrSb-$C2/c$, IrSb-$P\bar{1}$, $IrSb_2$-$P\bar{4}21m$, $IrSb_2$-$I4/mmm$ and Ir_2Sb-$Pmmn$ were identified at high pressures. The phonon dispersion curves reveal that these phases are all dynamically stable. The calculated electronic results show that a mixed behavior of covalent, ionic and metallic bonds simultaneously exits in these novel phases. A pressure-induced electronic topological transition in Ir_2Sb-$Pmmn$ phase occurs according to the theoretical electronic band structures, while is not shown in other stoichiometries of the Ir–Sb system. Our work provides a potential opportunity for experimental synthesis of crystal structures with different chemical stoichiometries of the binary Ir–Sb system.

Received 20th February 2020
Accepted 14th April 2020

DOI: 10.1039/d0ra01629b

rsc.li/rsc-advances

Introduction

Transition-metal compounds have aroused a great deal of interest from researchers due to their fundamental physics and as potential candidates for thermoelectric energy converters.[1–4] Binary transition-metal antimonides are considered as important functional materials exhibiting a range of potential applications for superconductivity and as lithium ion battery anode materials.[5–7] However, it is still a major challenge to experimentally synthesize transition-metal antimonides with novel structures and chemical stoichiometry in general under ambient conditions, because of the requirement for high temperatures and multi-step reactions under vacuum.[8,9] Fortunately, recent studies experimental synthesis has made several successes to synthesize several transition-metal antimonides, *e.g.*, arsenopyrite-type structure of $CoSb_2$,[10,11] skutterudite-type structure of $CoSb_3$,[12,13] nickel arsenide-type structure of NiSb and CoSb,[14,15] marcasite-type structure of $NiSb_2$,[16] and *anti*-PbCl-type structure of Cu_2Sb.[17]

High temperature phase diagram of intermetallic compounds Ir–Sb was reported in the 1950s based on metallographic, thermal and X-ray analyses.[18] The melting points were determined from cooling curves of alloys prepared from chemically pure components. Hexagonal NiAs-type IrSb was obtained according to metallographic observations of alloys after annealing 1500 K.[19] The melting point of $IrSb_2$ is higher than 1050 K, while $IrSb_3$ forms by a peritectic reaction of 1126 K.[20] Moreover, pressure induced irreversible isosymmetric transition of $IrSb_3$ by the X-ray diffraction up to 43 GPa have been reported.[21,22] Because of its relatively opened structure, it is expected to exhibit interesting behavior under high pressure. This void space can be filled with different atoms such as La or Ge to obtain the related family of compounds called filled skutterudites or stuffed skutterudites.[23] Filled skutterudite compounds have been considered as potential candidates for thermoelectric applications.[24,25] Interestingly, it could be interpreted as a pressure-induced self-insertion reaction which could be effectively improved the thermoelectric properties.

Utilizing the first-principle calculations combined with Boltzmann transport equation (BTE) and semiclassical analysis, high figure of merit zTs of 1.45 are obtained in n-type doped $IrSb_3$ at higher pressure.[26] These studies show that pressure plays a powerful role to tune the thermoelectric properties.[27] Thus, it is necessary to systematically investigate the crystal structure with various iridium antimonies stoichiometry and explore the corresponding bonding characterizes under high pressure.

[a]*Department of Physics, College of Science, Yanbian University, Yanji 133000, China. E-mail: yhliu@ybu.edu.cn*

[b]*School of Science, Changchun University of Science and Technology, Changchun 130000, China. E-mail: zhoudan777@aliyun.com*

[c]*Department of Materials Science, State Key Laboratory of Superhard Materials, Key Laboratory of Automobile Materials of MOE, Jilin University, Changchun 130000, China*

[d]*Department of Computer Science, College of Engineering, Yanbian University, Yanji 133000, China. E-mail: jinzhexue@ybu.edu.cn*

In this paper, we have explored the binary Ir–Sb phase diagram *via* a first-principles swarm-intelligence structure search and established a comprehensive understanding of the evolution of its crystal structures at 0–100 GPa. In addition to reproducing the known IrSb-$P6_3/mmc$, $IrSb_2$-$P2_1/c$ and $IrSb_3$-$Im\bar{3}$, the five novel high-pressure phases of Ir_2Sb-*Pmmn*, IrSb-*C*2/*c*, IrSb-$P\bar{1}$, $IrSb_2$-$P\bar{4}21m$ and $IrSb_2$-*I*4/*mmm* become energetically stable at 4.2 GPa, 16.4 GPa, 76.5 GPa, 45 GPa and 59.2 GPa, respectively. The electronic properties have been comprehensively investigated.[28,29] Interestingly, pressure-driven evolution of the electronic topology transitions in $IrSb_2$-*P*4/*nmm* phase has been confirmed. Furthermore, the pressure-induced different bonding characters are shown in these antimonies. Our result represents a significant step toward understanding the structural and electrical behavior of the binary Ir–Sb system under extreme condition.

Results and discussion

We have performed systematic structure prediction for Ir–Sb system by variable-cell simulation with cell sizes of 1–4 formula units (f.u.) at 0–100 GPa. The crystal structure with the lowest energy was predicted under different pressures, and the enthalpies formation of ΔH_f for the iridium antimonies stoichiometry can be obtained in the structure search at varying pressures, as shown in Fig. 1. The relative thermodynamic stability of different Ir–Sb compounds with respect to elemental solids Ir and Sb is calculated according to the following equation: $\Delta H_f(Ir_xSb_y) = [H(Ir_xSb_y) - xH(Ir) - yH(Sb)]/(x + y)$. In the formula, $H(Ir_xSb_y)$ represents the enthalpy of the structure in the range of stable pressure, and H(Ir) and H(Sb) represent the enthalpy of the Ir atom and the Sb atom at the corresponding pressure. Then, we construct the convex hull data for Ir–Sb system at each pressure. Solid star indicates thermodynamically stable phases and the unstable or meta-stable phases are expressed by hollow star.

The built pressure-composition phase diagram of the Ir–Sb system is shown in Fig. 2, with the stable structures identified using colors and space groups. At ambient pressure, the already known stoichiometries of $IrSb_3$-$Im\bar{3}$ and $IrSb_2$-$P2_1/c$ are well-reproduced in our structural search calculations in Fig. 3(a) and (b). However, it is to be found that experimental phase of the ground state IrSb (space group $P6_3/mmc$) tend to decompose into $IrSb_2$ phase in our pressure-composition phase diagram. Moreover, the optimized crystal parameters of $IrSb_2$ (space group $P2_1/c$) are $a = 6.734$ Å, $b = 6.675$ Å, $c = 6.831$ Å in good well with the experimental values of $a = 6.600$ Å, $b = 6.500$ Å, $c = 6.700$ Å, and that of in IrSb (space group $P6_3/mmc$) are $a = b = 4.082$ Å, $c = 5.634$ Å also consistent with the experimental values of $a = b = 3.978$ Å, $c = 5.521$ Å,[6–8] validating that our adopted structure searching method and PBE functional are applicable to the Ir–Sb system. No imaginary frequency is observed throughout the whole Brillouin zone, which indicates that the five novel phases are dynamically stable in the pressure region from this study, as shown in Fig. 4. The five novel phases of $IrSb_2$-$P\bar{4}21m$, $IrSb_2$-*I*4/*mmm*, IrSb-*C*2/*c*, IrSb-$P\bar{1}$ and Ir_2Sb-*Pmmn* are stable shown in Fig. 3(c)–(g) under high pressure and the crystal structure and physical properties of these structures will be examined in detail next. $IrSb_3$ is crystalized in a skutterudite-type structure, which can be also considered as a body centered cubic structure with a space group of $Im\bar{3}$ in Fig. 3(a). The antimonies atoms form planer, rectangular Sb_4 square with Sb–Sb distance of 3.033 Å. High-pressure calculations shows that the cubic $IrSb_3$-$Im\bar{3}$ will be stability up to 22.2 GPa.

At ambient pressure, the $IrSb_2$-$P2_1/c$ has a monoclinic symmetry in Fig. 3(b). Four Ir atoms and eight Sb atoms occupy the Wyckoff 4e site in the unit cell, respectively. In this structure, each Ir atom is coordinated to six Sb atoms in an octahedron environment, connected by an antimony bridge. The bond

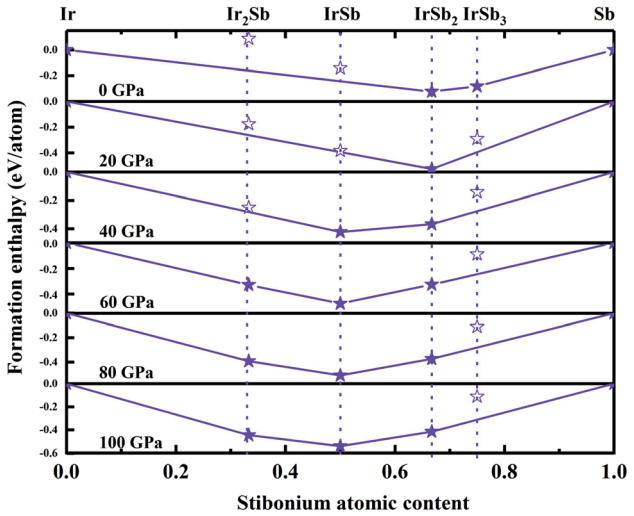

Fig. 1 Relative enthalpies of formation of Ir–Sb phase with respect to elemental iridium and stibonium solids. The convex hulls connecting stable phase (solid star) are shown by solid lines. Unstable/meta stable phase are shown by open star.

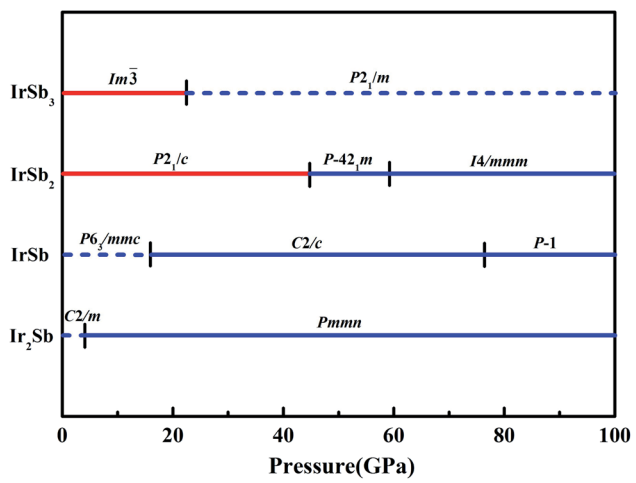

Fig. 2 Pressure-composition phase diagram of Ir–Sb compounds. Blue and red colors represent the metallic and insulating phases, respectively. The solid (dash) lines represent stable (metastable) phases.

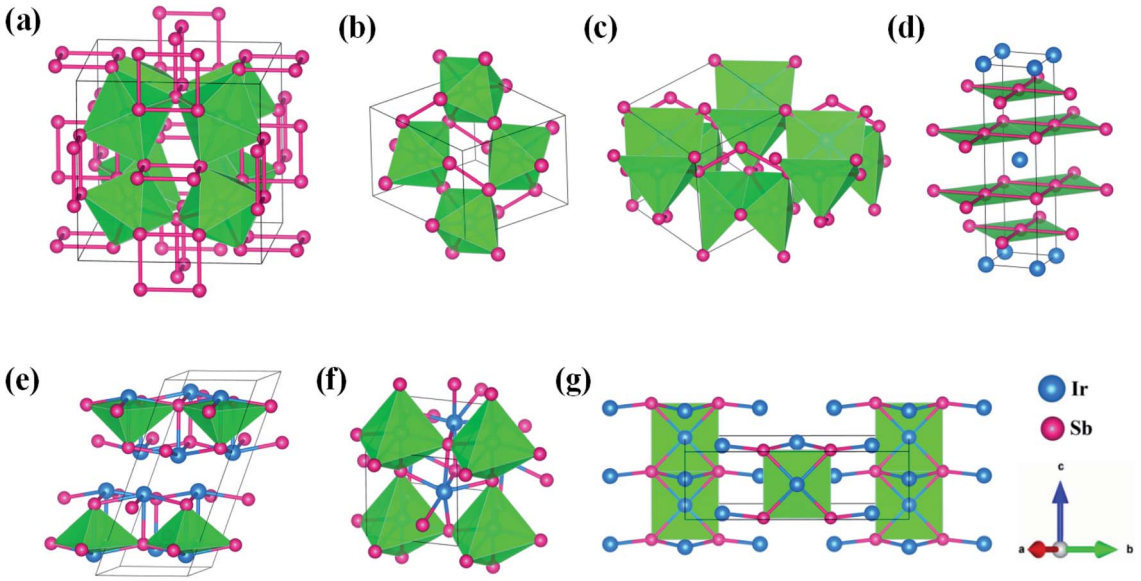

Fig. 3 Stable crystal structures of the considered Ir–Sb system for (a) $Im\bar{3}$ structure of $IrSb_3$, (b) $P2_1/c$ structure of $IrSb_2$, (c) $P\bar{4}21m$ structure of $IrSb_2$ (d) $I4/mmm$ structure of $IrSb_2$, (e) $C2/c$ structure of IrSb, (f) $P\bar{1}$ structure of IrSb and (g) $Pmmn$ structure of Ir_2Sb. The large (blue) and small (pink) spheres are Ir atom and Sb atom, respectively. The atomic positions are Ir at Wyckoff 8c (0.750, 0.250, 0.250) and Sb at 24g (0.500, 0.161, 0.346) for $Im\bar{3}$; the atomic positions are Ir at Wyckoff 4e (0.229, −0.000, 0.790) and Sb at 4e (0.844, 0.863, 0.823) and 4e (0.351, 0.635, 0.878) for $P2_1/c$; the atomic positions are Ir at Wyckoff 4e (0.676, 0.824, 0.227) and Sb at 4e (0.778, 0.722, 0.606), 2a (0.000, 0.000, 0.000) and 2c (0.500, 0.000, 0.858) for $P\bar{4}21m$; the atomic positions are Ir at Wyckoff 2a (0.000, 0.000, 0.000) and Sb at 4e (0.500, 0.500, 0.151) for $I4/mmm$; the atomic positions are Ir at Wyckoff 8f (0.400, 0.673, 1.361) and Sb at 8f (0.000, 0.500, 0.152) for $C2/c$; the atomic positions are Ir at Wyckoff 2i (0.217, 0.525, 0.204) and 2i (0.676, 0.877, 0.183) and Sb at 2i (0.200, 0.032, 0.297) and 2i (0.722, 0.393, 0.289) for $P\bar{1}$; the atomic positions are Ir at Wyckoff 2a (0.000, 0.000, 0.077), 2b (0.500, 0.000, 0.578) and 4e (0.000, 0.166, 0.612) and Sb at 4e (0.000, 0.350, 0.900) for $Pmmn$.

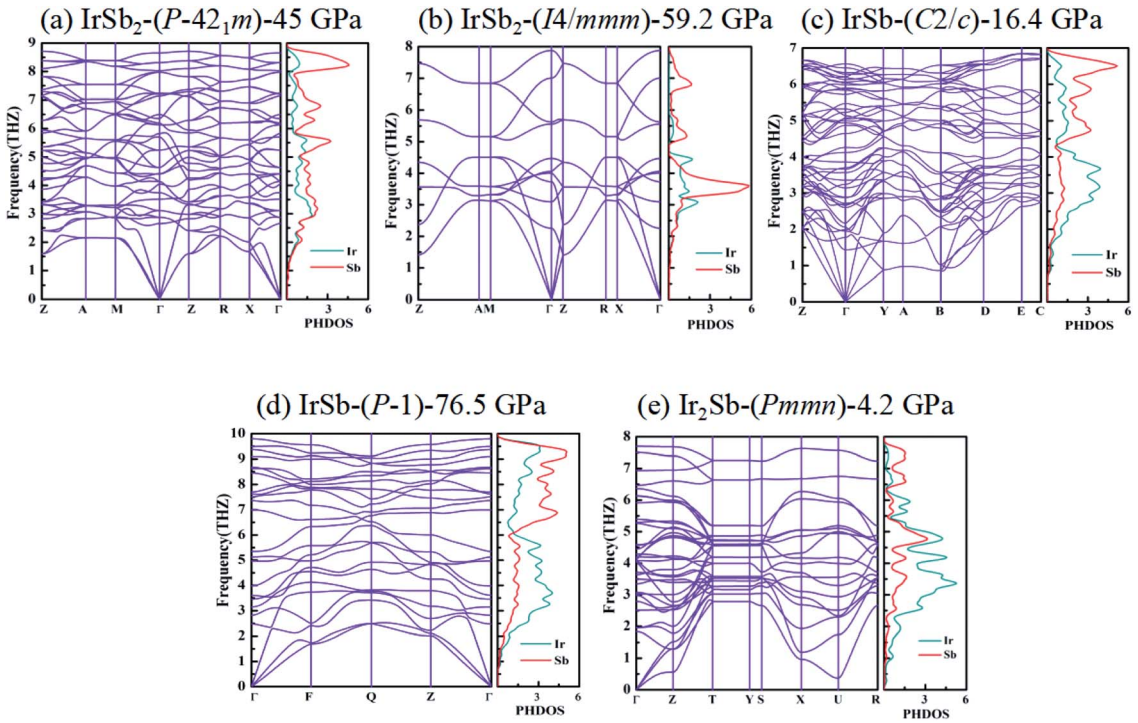

Fig. 4 Phonon-dispersion curves and PHDOS projected on Ir atoms and Sb atoms for (a) $IrSb_2$-$P\bar{4}21m$ at 45 GPa, (b) $IrSb_2$-$I4/mmm$ at 59.2 GPa, (c) IrSb-$C2/c$ at 16.4 GPa, (d) IrSb-$P\bar{1}$ at 76.5 GPa, and (e) Ir_2Sb-$Pmmn$ at 4.2 GPa.

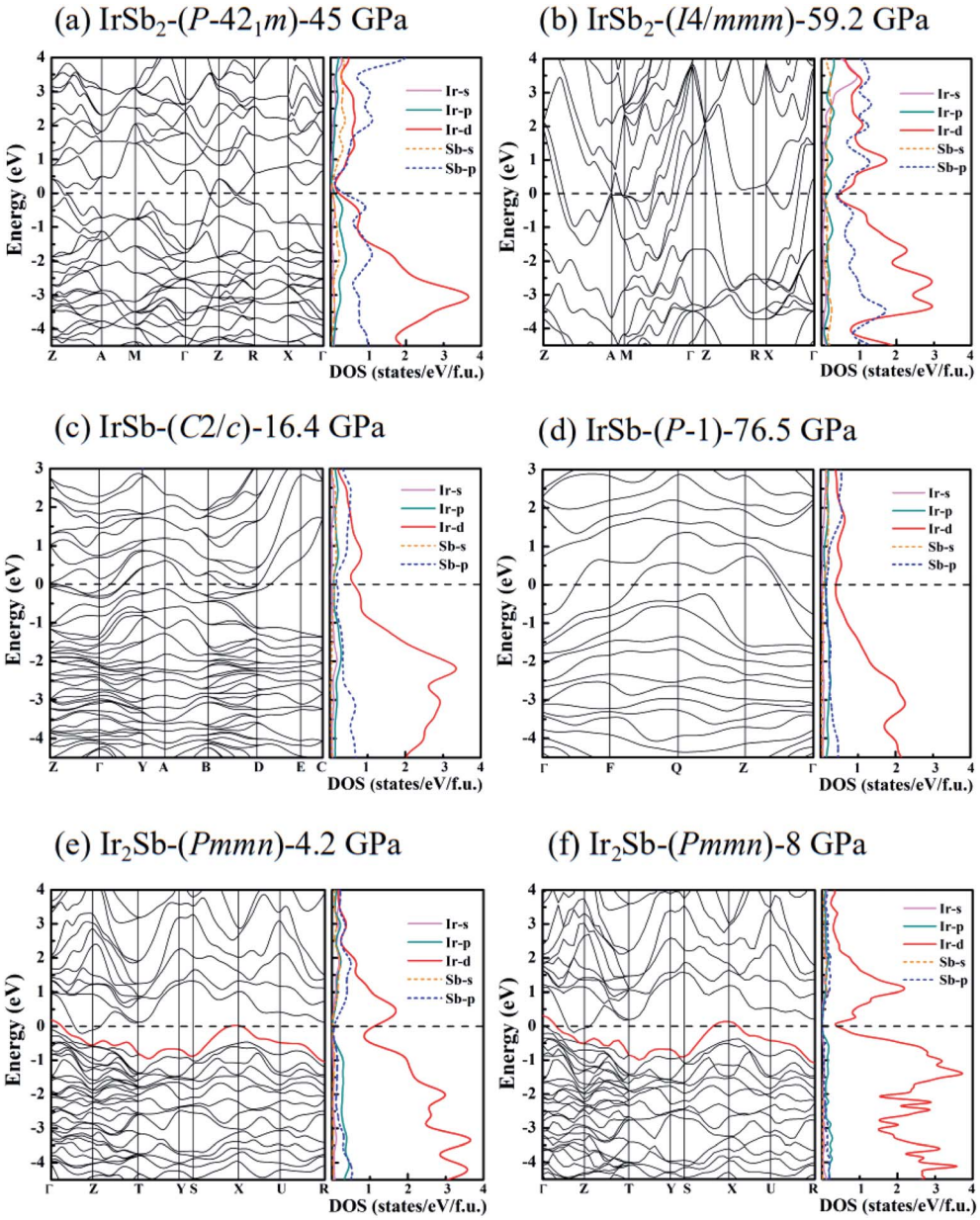

Fig. 5 Electronic band structure and the PDOS on Ir atoms and Sb atoms for (a) $IrSb_2$-$P\bar{4}21m$ at 45 GPa, (b) $IrSb_2$-$I4/mmm$ at 59.2 GPa, (c) IrSb-$C2/c$ at 16.4 GPa, (d) IrSb-$P\bar{1}$ at 76.5 GPa, (e) Ir_2Sb-$Pmmn$ at 4.2 GPa, and (f) Ir_2Sb-$Pmmn$ at 8 GPa. Note that zero energy is at the Fermi level.

length of Ir–Sb and Sb–Sb is 2.688 and 2.902 Å, respectively. At 45 GPa, the simulated $IrSb_2$-$P\bar{4}21m$ phase becomes more favorable, which has a tetragonal primitive symmetry with lattice parameters of $a = b = 5.854$ Å, and $c = 6.196$ Å in Fig. 3(c). In this case of the $IrSb_2$-$P\bar{4}21m$ phase, four Ir atoms occupy the wyckoff 4e site and six Sb atoms lie in 4e, 2a, and 2c sites in the unit cell, respectively. Each Ir atom is coordinated to five Sb atoms formed a quadrangular pyramid. Interestingly, the antimony atoms consist of Sb_3 unites with the Sb–Sb distance of 2.782 Å, which join the neighbor six quadrangular together. In the $IrSb_2$-$I4/mmm$ phase, it has a tetragonal primitive symmetry, its equilibrium lattice parameters are $a = b = 2.955$ Å, and $c = 11.218$ Å at 59.2 GPa in Fig. 3(d). Two Ir atoms occupy the Wyckoff 2a site and four Sb atoms lie in 4e site in the unit cell. The $IrSb_2$-$I4/mmm$ phase consists of alternate Ir and Sb layers atoms, with the Sb–Sb distance of 2.955 Å in the square layer, which is larger than that of 2.782 Å in $IrSb_2$-$P\bar{4}21m$.

The optimized structure of IrSb-$C2/c$ has a monoclinic structure at 16.4 GPa. At pressure of 76.5 GPa, the IrSb-$C2/c$ transforms into an anorthic IrSb-$P\bar{1}$ structure. In the IrSb-$C2/c$ phase, with lattice parameters of $a = 11.207$ Å, $b = 5.326$ Å, and $c = 5.061$ Å, and $\alpha = \gamma = 90.0°$, $\beta = 110.7°$ at 16.4 GPa in Fig. 3(e). Eight Ir atoms occupy the Wyckoff 8f site and eight Sb atoms lie in the 8f site in the unit cell. Each Ir atom is coordinated to five Sb atoms to form an octahedron in a unit cell. In the IrSb-$P\bar{1}$ phase, it belongs to a triclinic system, with lattice parameters of

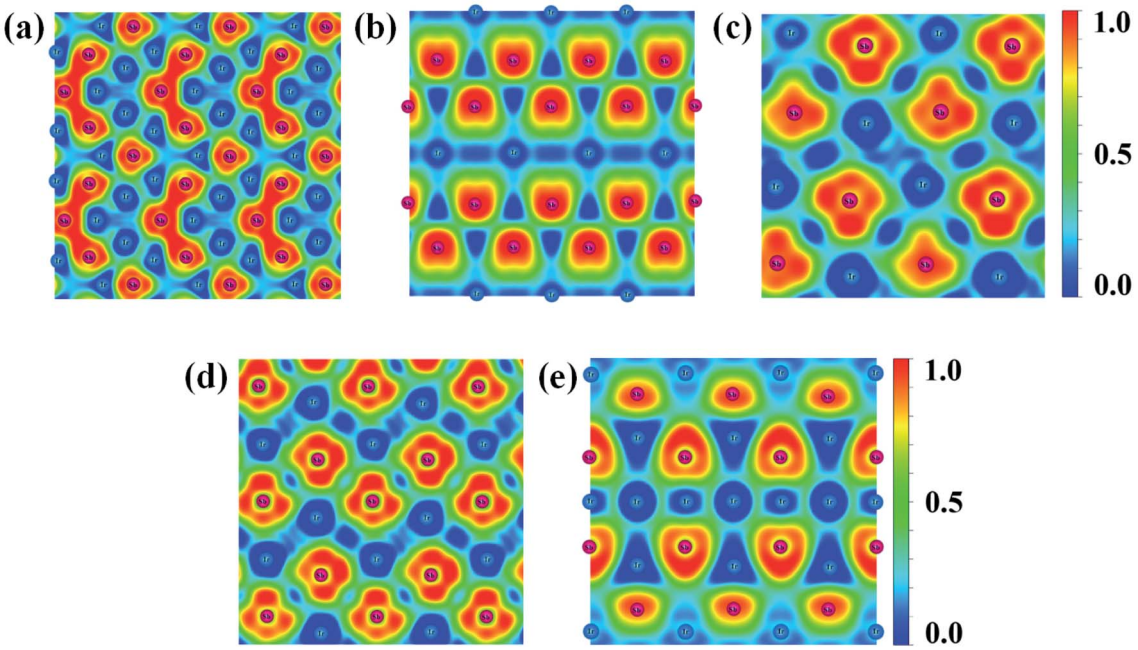

Fig. 6 Contours of the ELF for the structures of (a) $IrSb_2$-*P*42*1m*, (b) $IrSb_2$-*I*4/*mmm*, (c) IrSb-*C*2/*c*, (d) IrSb-*P*$\bar{1}$, and (e) Ir_2Sb-*Pmmn* with isosurface of 0.8.

$a = 4.812$ Å, $b = 5.034$ Å, and $c = 5.033$ Å, and $\alpha = 98.8°$, $\beta = 99.6°$, $\gamma = 92.1°$ at 76.5 GPa in Fig. 3(f). Four Ir atoms occupy the Wyckoff 2i site and four Sb atoms lie in the 2i site in the unit cell. Each Ir atom is coordinated to six Sb atoms to form an octahedral structure in a unit cell. The optimized structure of Ir_2Sb-*Pmmn* has a tetragonal structure at 4.2 GPa. In this structure, lattice parameters are $a = 3.874$ Å, $b = 12.479$ Å, and $c = 4.183$ Å at 4.2 GPa in Fig. 3(g). Eight Ir atoms occupy the Wyckoff 2a, 2b and 4e sites and four Sb atoms lie in the 4e site in the unit cell. Each Ir atom has adopted the four nearest neighboring Sb atoms forming planar structure. The refined cation–anion bond length is 2.740 Å. The current theoretical phonon dispersion curves and phonon density of states (PHDOS) have evidence of the absence of any imaginary dynamical vibration in the whole Brillouin zone for the novel five structures, as shown in Fig. 4.

To study the chemical bonding and electronic properties of the five novel phases of $IrSb_2$-*P*$\bar{4}$2*1m*, $IrSb_2$-*I*4/*mmm*, IrSb-C_2/c, IrSb-*P*$\bar{1}$ and Ir_2Sb-*Pmmn*, we have calculated the energy band structure, projected density of states (PDOS) and the electron localization function. As shown in the calculated PDOS (Fig. 5(a)–(e)), several electric bands cross the Fermi energy along high-symmetry directions in these structures. The results show the metallic characters for the five novel phases. Moreover, PDOS raises overlap between Sb 5p and Ir 5d orbitals below the Fermi level, indicating charge transfer from Sb 2p to Ir 5d. The electrons transferred are responsible for the relatively low difference of electronegativity of antimony (2.05) and iridium (2.20). The presence of strong Ir 5d component above the Fermi level indicates the depletion of 5d electrons in Ir atoms. This is further supported by the formation of Ir–Sb ionic bond by the electron localization function (ELF) analysis in Fig. 6(a)–(e).

A metallic Ir–Ir behavior can be observed near 0.5 ELF value. Moreover, the ELF appears Sb trimers in $IrSb_2$-*P*$\bar{4}$2*1m* is illustrated in Fig. 6(a).[30] The strong electron localization between Sb–Sb trimers indicates that the strong Sb–Sb covalent bonds bridged the Ir–Sb unites. The lack of electron density between Ir and Sb atom suggests extremely weak interactions between metal atoms in $IrSb_2$-*I*4/*mmm* (Fig. 6(b)). In Fig. 6(c)–(e), the information of Ir–Sb ionic bond and the electron localization around Sb atoms are shown in the ELF analysis.

We employ the Bader charge analysis, which provides a description of electron transfer, to quantify the amount of charge belonging to each atom at different stoichiometries.[31] The calculated charge amounts are 9.88 (4.56), 9.64 (4.68), 9.66 (4.34), 9.69 (4.30) and 9.43 (4.10) electron for Ir (Sb) in $IrSb_2$-*P*$\bar{4}$2*1m*, $IrSb_2$-*I*4/*mmm*, IrSb-C_2/c, IrSb-*P*$\bar{1}$ and Ir_2Sb-*Pmmn* phases, respectively. This results reveal that the charge states of Ir and Sb atoms change with pressure-induced transition and a peculiar reverse electron donation from Sb to Ir atoms. Accordingly, in Ir–Sb system, the bond between Ir and Sb atom shows evident ionic character and a little covalent bond exists between Ir and Sb atoms at the same time.

It is worth noting that an electronic topological transition can occur at doping, high pressure, temperature or other external reagents alter the Fermi surface of an electronic system that has significant impacts on the corresponding physical and chemical properties.[32,33] Therefore, we have checked the potential pressure-induced electronic topological transition in Ir_2Sb-*Pmmn*. As shown in Fig. 5(e), it is found that there is no band near the X point at 4.2 GPa. As the pressure increases, the

band moves down and approaches to the Fermi level at point X. Fig. 5(f) clearly shows that the red band along S–X–U is not fully occupied at 8 GPa and will form a hole pocket near the Fermi surface. Current theoretical predictions suggest that an electronic topological transition occurs in the Ir_2Sb-*Pmmn* structure.

In summary, the unbiased structure searching and density functional theory calculations are performed to explore the pressure-stabilized phases of Ir–Sb compounds under high pressure with a wide range of concentrations. Five novel phases of $IrSb_2$-$P\bar{4}21m$, $IrSb_2$-*I*4/*mmm*, IrSb-*C*2/*c*, IrSb-$P\bar{1}$ and Ir_2Sb-*Pmmn* were identified at high pressure. The theoretical phonon dispersion curves suggest that all these phases are dynamical stable. The calculated electronic band structures and density of states suggest that they are metallic. A pressure-induced electronic topological transition has been found in an Ir_2Sb phase. Accordingly, the electronic bonding states show evident covalent character in all of these five novel phases. The Bader charge analysis reveals that prominent electrons transfer from Ir to Sb atom in these novel phases are responsible for the ionic bonding feature of these compounds. The present findings establish the pressure-composition phase diagram of Ir–Sb system and corresponding electronic properties, which offer guidance for further fundamental understanding and experimental synthesis.

Methods

Structure prediction

Crystal structure prediction was performed at pressures of 0–100 GPa *via* an unbiased swarm intelligence based CALYPSO (Crystal structure AnaLYsis by Particle Swarm Optimization) method,[34–36] which was designed to search for the most stable or metastable structures of given compounds.[37–41]

First-principles calculations

Structural optimizations, electronic structure and phonon calculations, and molecular dynamics were performed in the framework of density functional theory (DFT). The generalized gradient approximation (GGA) expressed by the Perdew–Burke–Ernzerhof (PBE) functional[42] as implemented in the Vienna *Ab initio* Simulation Package (VASP)[43,44] was adopted. The electron–ion interaction was described by the projector augmented-wave potentials, with $5d^76s^2$ and $5s^25p^3$ configurations treated as valence electrons for Ir and Sb atoms are, respectively. The cutoff energy of 600 eV and Monkhorst–Pack scheme with a *k*-point grid of $2\pi \times 0.03$ Å^{-1} were adopted to obtain converged total energies (~1 meV per atom).[45,46] Phonon dispersions were calculated using the supercell approach as implemented in PHONOPY code with a displacement of 0.01 Å for all calculation. $2 \times 2 \times 2$, $4 \times 4 \times 1$, $1 \times 2 \times 2$, $2 \times 2 \times 2$, and $3 \times 1 \times 3$ supercells were found to be large enough for obtaining the converged dynamical matrixes for the $P\bar{4}21m$, *I*4/*mmm*, *C*2/*c*, $P\bar{1}$, and *Pmmn* structures, respectively.[47] For both heavy elements of Ir and antimony-containing systems relativistic shifts in the electron's atomic energy levels play a significant role.[48] Therefore, the spin orbital coupling (SOC) effect has been considered for the calculations of electronic band structures.

Data availability

The data that support the findings of this study are available from the corresponding author upon reasonable request.

Author contributions

Y. L. designed the research, S. L., D. Z. and Z. J. performed the calculations, Y. L., S. L., D. Z. and Z. J. analyzed the results and wrote the manuscript. All authors contributed to the discussions.

Conflicts of interest

The authors declare no competing financial or non-financial interests.

Acknowledgements

This work was supported by the Natural Science Foundation of China (11764043, 11704044, 11504007, and 11404035) and the Natural Science Foundation of Jilin Province, Science and Technology Development Project under No. 20180101226JC.

References

1 S. T. Oyama, *J. Solid State Chem.*, 1992, **96**, 442–445.
2 G. D. Mahan, B. C. Sales and J. W. Sharp, *Phys. Today*, 1997, **50**, 42–47.
3 F. J. DiSalvo, *Science*, 1999, **285**, 703–706.
4 T. Caillat, A. Borshchevsky and J. P. Fleurial, *AIP Conf. Proc.*, 1993, **271**, 771–776.
5 G. A. Slack and V. G. Tsoukala, *J. Appl. Phys.*, 1994, **76**, 1665–1671.
6 N. N. Zhuravlev, G. S. Zhdanov and R. N. Kuz'min, *Kristallografiya*, 1960, **5**, 553–562.
7 A. Kjekshus and T. Rakke, *Acta Chem. Scand., Ser. A*, 1977, **31**, 517–529.
8 A. Kjekshus, *Acta Chem. Scand.*, 1961, **15**, 678–681.
9 F. Hulliger, *Helv. Phys. Acta*, 1961, **34**, 782–786.
10 G. S. Zhdanov and R. N. Kuz'min, *Kristallografiya*, 1961, **6**, 872–881.
11 T. Siegrist and F. Hulliger, *J. Solid State Chem.*, 1986, **63**, 23–30.
12 N. N. Zhuravlev and G. S. Zhdanov, *Kristallografiya*, 1956, **1**, 509–513.
13 K. Koga, K. Akai, K. Oshiro and M. Matsuura, *20th ICT*, 2001, pp. 105–108.
14 U. Furst and F. Halla, *Z. Phys. Chem.*, 1938, **40**, 285–307.
15 T. Chen, J. C. Mikkelsen and G. B. Charlan, *J. Cryst. Growth*, 1978, **43**, 5–12.
16 A. Kjekshus, T. Rakke and A. F. Andresen, *Acta Chem. Scand.*, 1974, **28**, 996–1000.

17 M. Blander, G. Hagg and A. Westgren, *Arkiv for kemi mineralogi och geologi B*, 1935, **12**, 1–6.
18 R. N. Kuz'min, G. S. Zhdanov and N. N. Zhuravlev, *Kristallografiya*, 1957, **2**, 48–50.
19 R. N. Kuz'min, *Kristallografiya*, 1958, **3**, 366–367.
20 H. Okamoto, *J. Phase Equilib.*, 1994, **15**, 640–642.
21 T. Caillat, A. Borschevsky and J. P. Fleurial, *J. Alloys Compd.*, 1993, **199**, 207–210.
22 H. Okamoto, *J. Phase Equilib.*, 1994, **15**, 567–568.
23 S. W. Kim, Y. Kimura and Y. Mishima, *J. Electron. Mater.*, 2004, **33**, 1156–1160.
24 G. S. Nolas, D. T. Morelli and T. M. Tritt, *Annu. Rev. Mater. Sci.*, 1999, **29**, 89–116.
25 G. Chen, M. S. Dresselhaus, G. Dresselhaus, J. P. Fleurial and T. Caillat, *Int. Mater. Rev.*, 2003, **48**, 45–66.
26 X. X. Yang, Z. H. Dai, Y. C. Zhao, W. C. Niu, J. Y. Liu and S. Meng, *Phys. Chem. Chem. Phys.*, 2019, **21**, 851–858.
27 S. Y. Lin, M. L. Xu, J. Hao, X. L. Wang, M. Wu, J. M. Shi, W. W. Cui, D. Liu, W. W. Lei and Y. W. Li, *J. Mater. Chem. C*, 2019, **7**, 4527–4532.
28 C. Wang, Y. X. Liu, X. Chen, P. Lv, H. R. Sun and X. B. Liu, *Chin. Phys. Lett.*, 2020, **37**, 026201–026205.
29 S. Q. Jiang, X. Yang, X. L. Huang, Y. P. Huang, X. Li and T. Cui, *Chin. Phys. Lett.*, 2020, **37**, 016302–016306.
30 A. D. Becke and K. E. Edgecombe, *J. Chem. Phys.*, 1990, **92**, 5397–5403.
31 R. F. W. Bader, *Acc. Chem. Res.*, 1985, **18**, 9–15.
32 D. Zhou, Q. Li, Y. M. Ma, Q. L. Cui and C. F. Chen, *J. Phys. Chem. C*, 2013, **117**, 12266–12271.
33 X. J. Ma, X. Li, D. Zhou, J. Xu, W. Q. Gao and Y. H. Liu, *J. Alloys Compd.*, 2019, **791**, 1257–1262.
34 Y. C. Wang, J. Lv, L. Zhu and Y. M. Ma, *Comput. Phys. Commun.*, 2012, **183**, 2063–2070.
35 Y. C. Wang, J. Lv, L. Zhu and Y. M. Ma, *Phys. Rev. B: Condens. Matter Mater. Phys.*, 2010, **82**, 094116–094124.
36 H. Wang, Y. C. Wang, J. Lv, Q. Li, L. J. Zhang and Y. M. Ma, *Comput. Mater. Sci.*, 2016, **112**, 406–415.
37 C. Y. Zhu, X. Qu, M. Zhang, J. Y. Wang, Q. Li, Y. Geng, Y. M. Ma and Z. M. Su, *J. Mater. Chem. A*, 2019, **7**, 13356–13363.
38 G. T. Zhang, R. Gao, Y. R. Zhao, T. T. Bai and Y. F. Hu, *J. Alloys Compd.*, 2017, **723**, 802–810.
39 X. Q. Song, K. T. Yin, Y. C. Wang, A. Hermann, H. Y. Liu, J. Lv, Q. Li, C. F. Chen and Y. M. Ma, *J. Phys. Chem. Lett.*, 2019, **10**, 2761–2766.
40 Q. Li, D. Zhou, W. T. Zheng, Y. M. Ma and C. F. Chen, *Phys. Rev. Lett.*, 2013, **110**, 136403–136407.
41 D. Zhou, Q. Li, W. T. Zheng, Y. M. Ma and C. F. Chen, *Phys. Chem. Chem. Phys.*, 2017, **19**, 4560–4566.
42 J. P. Perdew, K. Burke and M. Ernzerhof, *Phys. Rev. Lett.*, 1996, **77**, 3865–3868.
43 G. Kresse and J. Hafnerr, *Phys. Rev. B: Condens. Matter Mater. Phys.*, 1994, **49**, 14251–14269.
44 G. Kresse and J. Hafnerr, *Phys. Rev. B: Condens. Matter Mater. Phys.*, 1993, **47**, 558–561.
45 H. J. Monkhorst and J. D. Pack, *Phys. Rev. B: Condens. Matter Mater. Phys.*, 1976, **13**, 5188–5192.
46 D. Thirumalai, R. W. Hall and B. J. Berne, *J. Chem. Phys.*, 1984, **81**, 2523–2527.
47 A. Togo, F. Oba and I. Tanaka, *Phys. Rev. B: Condens. Matter Mater. Phys.*, 2008, **78**, 134106–134115.
48 G. Y. Gao, R. Hoffmann, N. W. Ashcroft, H. Y. Liu, A. Bergara and Y. M. Ma, *Phys. Rev. B: Condens. Matter Mater. Phys.*, 2013, **88**, 184104–184117.